


Higher-order topological superconductor phases in a multilayer system

Ryota Nakai and Kentaro Nomura

Department of Physics, Kyushu University, Fukuoka 819-0395, Japan (Received 7 August 2023; revised 5 November 2023; accepted 6 November 2023; published 30 November 2023)

Higher-order topological phases are gapped phases of matter that host gapless corner or hinge modes. For the case of superconductors, corner or hinge modes are gapless Majorana modes or Majorana zero modes. To construct three-dimensional higher-order topological superconductors, we consider a topological-insulator/superconductor multilayer under in-plane Zeeman coupling. We found three different types of higher-order topological superconductor phases, a second-order topological superconductor phase with Majorana hinge flat bands, a second-order Dirac superconductor phase with surface Majorana cones and Majorana hinge arcs, and nodal-line superconductor phases with drumhead surface states and Majorana hinge arcs.

DOI: [10.1103/PhysRevB.108.184517](https://doi.org/10.1103/PhysRevB.108.184517)**I. INTRODUCTION**

Topological insulators (TIs) and topological superconductors (TSCs) are electronic systems that have a gapped bulk spectrum and gapless boundary modes. These systems have been initially classified by the Altland-Zirnbauer symmetry class by the presence/absence of time-reversal, particle-hole, and chiral symmetries [1,2]. Beyond this classification, topological semimetals [3–6] that have gapless bulk nodes, topological crystalline insulators [7,8] that are protected by crystalline symmetries, and their corresponding superconductors (SCs) [9–14] have been widely studied.

Topological systems show quantized responses directly related to the topological numbers of the electronic states in filled bands. In two dimensions, quantum Hall, quantum anomalous Hall (QAH), quantum spin Hall (QSH), and TSC systems show the quantized (electric, spin, thermal) Hall conductivity [15–17]. In one dimension, electronic systems with inversion symmetry have a quantized dipole moment [18–21]. The concept of the dipole-moment quantization has been extended to the multipole quantization such as quadrupole and octupole moments [22,23]. Electronic systems hosting quantized multipole moments are known as higher-order TIs [22–26]. Multipoles are quantized in the presence of crystalline symmetry such as reflection, rotation, and inversion [27], and hence the higher-order TIs are topological crystalline insulators beyond the conventional classification of topological insulators. In general, n th-order TIs host gapless modes in a $(d - n)$ -dimensional subspace, where d is the material's dimensions. Specifically, while first-order TIs are usual TIs, second-order TIs have corner zero modes in two dimensions and gapless hinge modes in three dimensions. Higher-order topological phases has been confirmed in photonic systems [28–30].

Of particular interest are the higher-order topological superconductors (HOTSCs) [31–60] as they host localized Majorana zero modes, which can be utilized in quantum computation [61]. Specifically, two-dimensional (2D) second-order topological superconductor (SOTSC) phases have been predicted in heterostructures such as the 2D TI/ d -wave or

s_{\pm} -wave SC [37,62,63], second-order TI/SC [40,64], $p \pm ip/d$ -wave SCs [35], 3D antiferromagnetic TI/SC [38], 2D TI/ s -wave SC under an in-plane magnetic field [65–69], Rashba-metal/ $s + id$ -wave SC [70,71], a π junction of SC/QSH-bilayer/SC [72], and so on. However, not as much is known about the construction of 3D HOTSC phases by heterostructures.

For the construction of novel three-dimensional topological phases, one possible route is to make a multilayer structure of topological materials and other gapped materials. This strategy has been adopted for creating Weyl semimetal (WSM) phases by multilayers of a TI/trivial insulator and WSM/trivial insulator [5,73]. The method has been applied to multilayers of SC/TI and SC/WSM to construct Weyl superconductor (WSC) phases [10,74], which have point nodes in the bulk superconducting states and Majorana Fermi arcs on the surface. Recently, a π junction through two Rashba-metal layers under an in-plane magnetic field has been predicted to be a 2D SOTSC [75]. This system is similar to a part of the SC/TI multilayer, as both systems require a π junction (π -phase difference) between neighboring SCs [10]. So it is natural to expect that a multilayer of SC and TI under an in-plane magnetic field shows 3D HOTSC phases.

In this work, we study a multilayer of TI and conventional SC forming a π junction under in-plane Zeeman coupling [Fig. 1 (right)]. The phase difference between neighboring SC layers can be tuned by a magnetic flux inserted through a Josephson junction whose endpoints are connected to the SC layers (not explicit in Fig. 1 (right); see [10,76]). Let us see what could happen under in-plane Zeeman coupling. When the Zeeman field aligns the out-of-plane direction, WSC phases appear between weak TSC phases whose sections (let us say normal to the k_z axis) in the momentum space have nontrivial Chern numbers [10]. By flipping the Zeeman field, the sign of the Chern number is reversed. With this mechanism, when the Zeeman field is tilted to the in-plane direction, weak TSC phases turn to nodal-line superconductor (NLSC) phases by closing a bulk gap at each k_z . Similarly, the WSC phases also turn to NLSC phases, where nodes in a WSC phase are connected by nodal lines. In addition to NLSC

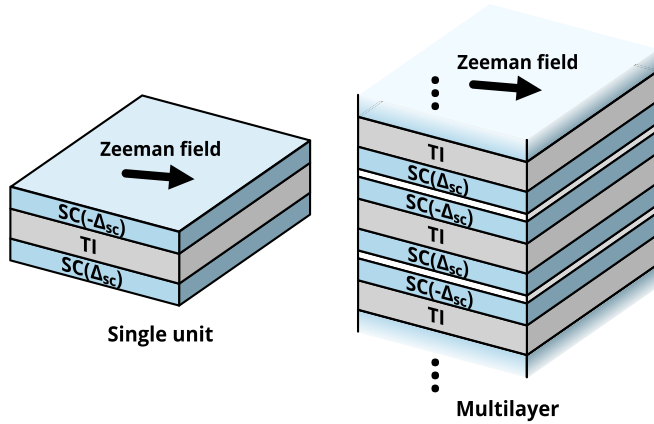


FIG. 1. A single unit of superconductor(SC)/topological insulator(TI)/SC layers and a multilayer model of TI/SC under in-plane Zeeman coupling. In the multilayer model, each SC layer consists of two SC layers [SC(Δ_{SC}) and SC($-\Delta_{SC}$)] forming a π junction separated by an insulator layer.

phases, we found a 3D SOTSC phase and a second-order Dirac superconductor (SODSC) phase [45]. The 3D SOTSC is a bulk-gapped SC where the k_z section is a 2D SOTSC. The SODSC is a bulk-gapped SC where the k_z section is either a 2D SOTSC or a trivial SC, and surface Majorana point nodes separate them. The emergence of SOTSC phases in this multilayer system has been overlooked in previous works as these phases cannot be deduced from bulk and surface spectra. In addition, we found that NLSC phases that appear next to the 3D SOTSC phase have both drumhead surface states and Majorana hinge states forming a flat band.

This paper is organized as follows. We first study effective low-energy models of a TI/SC multilayer under in-plane Zeeman coupling in Sec. II. We review the case with a single layer and thoroughly study the π -junction case as these results are used in the multilayer case. Then we study the effective multilayer model. To make the presence of Majorana hinge modes clear, we numerically study a lattice multilayer model in Sec. III. Similarly to the previous section, we start with a detailed study of a single-layer model and then move on to the multilayer case. We finally conclude in Sec. IV.

II. EFFECTIVE SURFACE MODEL

First, we consider an effective model, in which only the surface Dirac fermions of the 3D TI layer are taken into account as an effective low-energy theory. SCs are incorporated as an induced pair potential by the proximity effect.

A. Single unit

Let us discuss a single unit case, that is, a single TI layer sandwiched by two SCs [Fig. 1 (left)]. This system is similar to models studied in [68,75,77], but we will review in particular the SOTSC phase and the corner Majorana modes in detail, aiming to extend to the multilayer system. The effective

Hamiltonian reads

$$H = \sum_{\mathbf{k}_\perp} [c_{\mathbf{k}_\perp}^\dagger \mathcal{H}_0(\mathbf{k}_\perp) c_{\mathbf{k}_\perp} + c_{\mathbf{k}_\perp}^\dagger \mathcal{H}_\Delta(\mathbf{k}_\perp) c_{-\mathbf{k}_\perp}^\dagger + \text{H.c.}],$$

$$\mathcal{H}_0(\mathbf{k}_\perp) = v_F (\hat{z} \times \boldsymbol{\sigma}) \cdot \mathbf{k}_\perp \rho^z + t_s \rho^x + \Delta_Z \mathbf{n} \cdot \boldsymbol{\sigma},$$

$$\mathcal{H}_\Delta(\mathbf{k}_\perp) = i \Delta_{SC} \sigma^y (\cos \varphi / 2 + i \rho^z \sin \varphi / 2), \quad (1)$$

where $c_{\mathbf{k}_\perp} = (\psi_{\mathbf{k}_\perp \text{top}\uparrow}, \psi_{\mathbf{k}_\perp \text{top}\downarrow}, \psi_{\mathbf{k}_\perp \text{bottom}\uparrow}, \psi_{\mathbf{k}_\perp \text{bottom}\downarrow})$, $\mathbf{k}_\perp = (k_x, k_y)$ is the momentum along the TI surface, σ and ρ are the Pauli matrices for the spin and top/bottom-surface degrees of freedom, respectively, v_F is the Fermi velocity of the surface Dirac fermion, and \hat{z} is the unit vector normal to the surfaces. Δ_{SC} is the induced pair potential and φ is the phase difference between the pair potential from the top and bottom SCs. Δ_Z is the magnitude of Zeeman coupling and \mathbf{n} is the orientation of the Zeeman field. The intralayer tunneling amplitude between the top and bottom surfaces of the 3D TI is t_s .

In the Nambu space, the total Hamiltonian reads

$$\mathcal{H}_{\text{single}}(\mathbf{k}_\perp) = v_F (-k_x \sigma^y \rho^z \tau^z + k_y \sigma^x \rho^z) + t_s \rho^x \tau^z$$

$$+ \Delta_Z (n_x \sigma^x \tau^z + n_y \sigma^y + n_z \sigma^z \tau^z)$$

$$- \Delta_{SC} \sigma^y (\tau^y \cos \varphi / 2 + \rho^z \tau^x \sin \varphi / 2), \quad (2)$$

where τ is the Pauli matrix acting on the Nambu space. This model is invariant under particle-hole conjugation by $\mathcal{P} = \tau^x \mathcal{K}$, where \mathcal{K} is the complex conjugation operator. Provided the phase difference is either 0 or π and Zeeman coupling is absent, the model is invariant under time reversal by $\Theta = i \sigma^y \mathcal{K}$ when $\varphi = 0$ and $\Theta = i \sigma^y \tau^z \mathcal{K}$ when $\varphi = \pi$ [77]. Regarding crystalline symmetry, the model without Zeeman coupling has mirror symmetry $M_x = \sigma^x \tau^z$ and $M_y = \sigma^y$ with respect to the plane normal to the x and y axes, respectively, and fourfold rotational symmetry $U_4 = e^{i\pi \sigma^z \tau^z / 4}$ with respect to the z axis. Notice that Zeeman coupling can break the mirror and rotational symmetries mentioned above. Combining mirror symmetry $M_z = \sigma^z \rho^x \tau^x$ with respect to the plane normal to the z axis, the total Hamiltonian is invariant under 3D inversion, $I = M_x M_y M_z \propto \rho^x$.

Let us first discuss the phase diagram without Zeeman coupling ($\Delta_Z = 0$). Without the proximity effect ($\Delta_{SC} = 0$), a thin TI layer is a quantum spin Hall (QSH) insulator [78]. When the proximity effect is turned on, the bulk phase depends on the phase difference φ . The bulk spectrum has an energy gap $(t_s^2 + \Delta_{SC}^2 \pm 2t_s \Delta_{SC} \sin \varphi / 2)^{1/2}$. For the 0 junction ($\varphi = 0$), the energy gap $(t_s^2 + \Delta_{SC}^2)^{1/2}$ indicates that there is no phase transition between the t_s -dominated region (QSH) and the Δ_{SC} -dominated region, and thus the resulting phase is a trivial SC phase. From the edge perspective, the helical edge modes in QSH disappear by an energy gap induced by the proximity effect [79]. On the other hand, for the π junction ($\varphi = \pi$), the energy gap is $t_s \pm \Delta_{SC}$, which indicates a topological phase transition at $|\Delta_{SC}| = |t_s|$. The phase with $\Delta_{SC}/t_s > 1$ is the helical TSC phase which is protected by time-reversal symmetry [77]. When the phase difference is slightly changed from $\varphi = \pi$, the helical TSC phase disappears as time-reversal symmetry is broken.

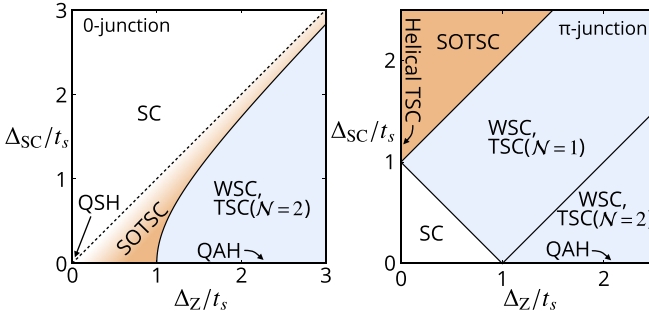


FIG. 2. The phase diagrams of a single unit of a SC/TI/SC Josephson junction, where the phase difference is 0 (left) and π [right, see Fig. 1 (left)], in Δ_Z - Δ_{SC} space. Large Zeeman coupling regions ($\Delta_Z \gg \Delta_{SC}$) are dominated by topological superconductor (TSC) phases when an out-of-plane Zeeman field is applied and Weyl superconductor (WSC) phases when in plane. A second-order topological superconductor (SOTSC) phase with two Majorana corner modes appears in the large pair-potential region ($\Delta_Z \ll \Delta_{SC}$) in a π junction.

Including Zeeman coupling in the 0 junction, the spectrum is given by

$$\epsilon^2 = v_F^2(k_x^2 + k_y^2 \cos^2 \theta) + (\Delta_Z \pm \sqrt{v_F^2 k_y^2 \sin^2 \theta + t_s^2 + \Delta_{SC}^2})^2, \quad (3)$$

where $\mathbf{n} = (\sin \theta, 0, \cos \theta)$. All states are doubly degenerate. Unless the Zeeman field is oriented in plane ($\theta \neq \pi/2$), the energy gap closes at $\mathbf{k}_\perp = (0, 0)$ when $\Delta_Z = \pm(t_s^2 + \Delta_{SC}^2)^{1/2}$. The phase diagram is shown in Fig. 2 (left). The Zeeman-coupling-dominated phase is a time-reversal-symmetry-broken TSC phase with the Bogoliubov–de Gennes Chern number $\mathcal{N} = \pm 2$. The Chern number is determined by the sign of the z component of the Zeeman field ($\text{sign}[\Delta_Z n_z]$). Hence, when the Zeeman field aligns the in-plane direction ($\theta = \pi/2$), the Zeeman-coupling-dominated phase is the topological phase transition point between the TSC phases with $\mathcal{N} = 2$ and -2 . This phase is a 2D WSC phase, which has point nodes in the bulk. Notice that the energy gap of the helical edge mode opened by the proximity effect can be closed and reopened by Zeeman coupling. When Zeeman coupling works at different magnitudes for different edges in a rectangular geometry, corner Majorana modes could appear between Δ_{SC} -dominated and Δ_Z -dominated edges [79]. This phase is a SOTSC phase with four corner Majorana modes [66]. However, the appearance of these corner Majorana modes depends on the orientation of the Zeeman field and does not accompany a bulk topological phase transition as this is solely an edge phenomenon. This phase is not the focus of this study.

On the other hand, including Zeeman coupling in a π junction, the eigenenergy is given by

$$\epsilon^2 = v_F^2(k_x^2 + k_y^2 \cos^2 \theta) + (\Delta_Z \pm \sqrt{v_F^2 k_y^2 \sin^2 \theta + (t_s \pm \Delta_{SC})^2})^2. \quad (4)$$

Unless in plane ($\theta \neq 0$), there are topological phase transitions at $\Delta_Z = \pm t_s \pm \Delta_{SC}$ [Fig. 2 (right)]. Between the TSC

phase with $\mathcal{N} = 2$ (continuously connected to the QAH phase) and the SC phase, a TSC phase with $\mathcal{N} = 1$ appears, which is similar to Ref. [80]. Similarly to the 0-junction case, when the Zeeman field aligns the in-plane direction, TSC phases become WSC phases. The focus of this study is the SOTSC phase when Δ_{SC} is dominated.

Let us analyze this phase from the edge perspective following Ref. [77]. Without Zeeman coupling, the helical TSC phase has helical Majorana edge modes that are protected by time-reversal symmetry. Consider an edge at $y = 0$ where the bulk is in $y > 0$. The helical Majorana modes with $k_x = 0$ are the solution of $\mathcal{H}_{\text{single}}(0, -i\partial_y)\psi(y) = 0$ by slightly changing the tunneling term as $t_s \rightarrow t_s - B\partial_y^2$ ($B > 0$). To satisfy the boundary condition $\psi(y = 0) = 0$ and $\psi(y \rightarrow \infty) = 0$, the equation is solved with an ansatz wave function,

$$\psi(y) \propto (e^{-\eta_+ y} - e^{-\eta_- y})\phi, \quad (5)$$

where ϕ is an eight-component spinor. Two solutions $\psi^{\text{R/L}}(y)$ are present provided $\Delta_{SC} > t_s$ and are given by $\eta_\pm = \{v_F \pm [v_F^2 + 4B(t_s - \Delta_{SC})]^{1/2}\}/2B$ with eigenspinors $\phi = \phi^{\text{R/L}}$, respectively. Since ϕ^{R} (ϕ^{L}) is the eigenvector of $-v_F k_x \sigma^y \rho^z \tau^z$ with eigenvalues $v_F k_x$ ($-v_F k_x$), these correspond to the helical Majorana edge modes.

The helical Majorana modes are gapped by Zeeman coupling [34,75]. Since $\langle \phi^{\text{R}} | \sigma^x \tau^z | \phi^{\text{L}} \rangle = i$, the x component of the Zeeman coupling opens a gap. The gap is finite unless the Zeeman field is perpendicular to the edge, and the sign of the gap depends on the relative direction between the Zeeman field and the edge. The orientation of the edge is defined in the counterclockwise direction around the bulk. In a rectangular geometry, the sign of the gap changes at two corners provided that the in-plane Zeeman field is not parallel to any of the edges. These corners can be viewed as domain walls where the sign of the gap changes and thus bind corner Majorana zero modes [75]. Since the mass induced by in-plane Zeeman coupling is odd under twofold rotational symmetry C_2 , the presence of the corner Majorana zero modes is guaranteed in rectangular geometry [27,34,39]. This phase is a 2D SOTSC phase with two Majorana corner modes.

B. Multilayer

Next, we extend the model in the previous section to a multilayer model by stacking TI and SC layers repeatedly [Fig. 1 (right)]. The case in which the Zeeman field aligns the out-of-plane (z) direction has been studied in [10]. The low-energy effective Hamiltonian is given by

$$H = \sum_{i,j,\mathbf{k}_\perp} \Psi_{i\mathbf{k}_\perp}^\dagger \mathcal{H}_{ij}(\mathbf{k}_\perp) \Psi_{j\mathbf{k}_\perp}, \quad (6)$$

where i, j are the index of the TI layers, $\mathbf{k}_\perp = (k_x, k_y)$, and $\Psi_{i\mathbf{k}_\perp} = (c_{i\mathbf{k}_\perp}, c_{i-\mathbf{k}_\perp}^\dagger)$. The Hamiltonian of each TI layer is the same as the one in the previous section [Eq. (2)], and the tunneling terms couple neighboring layers as

$$\mathcal{H}_{ij}(\mathbf{k}_\perp) = \mathcal{H}_{\text{single}}(\mathbf{k}_\perp) \delta_{ij} + \frac{t_d}{2} (\delta_{i,j+1} \rho^- + \delta_{i,j-1} \rho^+) \tau^z. \quad (7)$$

By Fourier transform in the z direction, we obtain the Hamiltonian in the momentum space,

$$\mathcal{H}(\mathbf{k}) = \mathcal{H}_{\text{single}}(\mathbf{k}_\perp) + t_d (\cos k_z \rho^x \tau^z + \sin k_z \rho^y \tau^z), \quad (8)$$

where $\mathbf{k} = (k_x, k_y, k_z)$. This model has the same symmetries as the single-unit model, that is, particle-hole and inversion symmetries, while time-reversal, fourfold rotational, and mirror symmetries are broken by Zeeman coupling.

In the following, we focus on the π phase difference and the x component of the Zeeman field. Comparing Eqs. (2) and (8), the Hamiltonian of the multilayer model at $k_z = 0$ and π is the same as that of the single layer by replacing intralayer coupling by $t_s \rightarrow t_s + t_d$ and $t_s - t_d$, respectively. So, we can deduce the phase diagram of the multilayer model from the single-layer results. In the following, we assume $t_s > t_d > 0$, but the other case can be discussed in the same way.

Without Zeeman coupling, the phase with $\Delta_{SC} > t_s + t_d$ has helical Majorana surface modes in the entire k_z space ($k_z \in [-\pi, \pi]$). This phase is a 3D helical TSC phase, each k_z section of which is a 2D helical TSC. On the other hand, in the phase with $\Delta_{SC} \in [t_s - t_d, t_s + t_d]$, helical Majorana surface modes are present at $k_z = \pi$, but absent at $k_z = 0$. This indicates a helical Majorana Fermi arc on the surface and Weyl nodes in the bulk. This is a 3D WSC phase [Fig. 3(b)].

Including Zeeman coupling along x direction, the helical TSC phase becomes a 3D SOTSC phase as an energy gap opens in the helical Majorana surface modes. Majorana hinge modes form a flat band at $\epsilon = 0$. What is interesting in this model is the appearance of NLSC phases, which has no correspondence in the single-unit model [Fig. 3(c)]. By increasing Zeeman coupling, the 3D SOTSC phase turns to an NLSC phase as the 2D SOTSC phase at the $k_z = 0$ section turns to a 2D WSC phase [see Fig. 2 (right)]. Let us check the bulk energy spectrum. Here we consider the spectrum at $k_x = 0$,

$$\epsilon(k_x = 0, k_y, k_z) = \pm \Delta_Z \pm \left[(v_F k_y)^2 + (\Delta_{SC} \pm \sqrt{t_s^2 + t_d^2 \pm 2t_s t_d \cos k_z})^2 \right]^{1/2}. \quad (9)$$

Nodal line(s) appears in the k_y - k_z plane. The condition of the appearance of the bulk nodes is $|\Delta_Z| > |\Delta_{SC} \pm (t_s^2 + t_d^2 \pm 2t_s t_d \cos k_z)^{1/2}|$. Nodal lines are present in the region where this condition is satisfied. The phase diagram on Δ_{SC} - Δ_Z space is shown in Fig. 3(a). Along the dashed lines, the geometrical feature of the nodal-line shape changes. Notice that as the orientation of the Zeeman field deviates from the in-plane direction, nodal lines are gapped out except at $\mathbf{k}_\perp = (0, 0)$ and becomes a 3D WSC phase [10]. In the limit of $\Delta_{SC} = 0$, two nodal lines close to each other fuse and become a nodal-line semimetal (NLSM) [(V) and (VII) phases in Fig. 3(a)].

Specifically, in phase (I) in Fig. 3(a), Zeeman coupling turns the bulk nodes into bulk nodal lines [Fig. 3(b) into Fig. 3(c)]. The nodal lines accompany drumhead states inside loops that are the projection of the bulk nodal lines onto the surface. These drumhead states are bound to the surface. Now the helical Majorana Fermi arc disappears as Zeeman coupling opens a gap. Instead, zero modes appear at the hinge. The Majorana hinge modes form a flat band in part of the Brillouin zone along k_z , whose endpoints are at the edges of the drumhead states [Fig. 3(c)]. An explicit form of the wave function of the Majorana hinge modes can be obtained

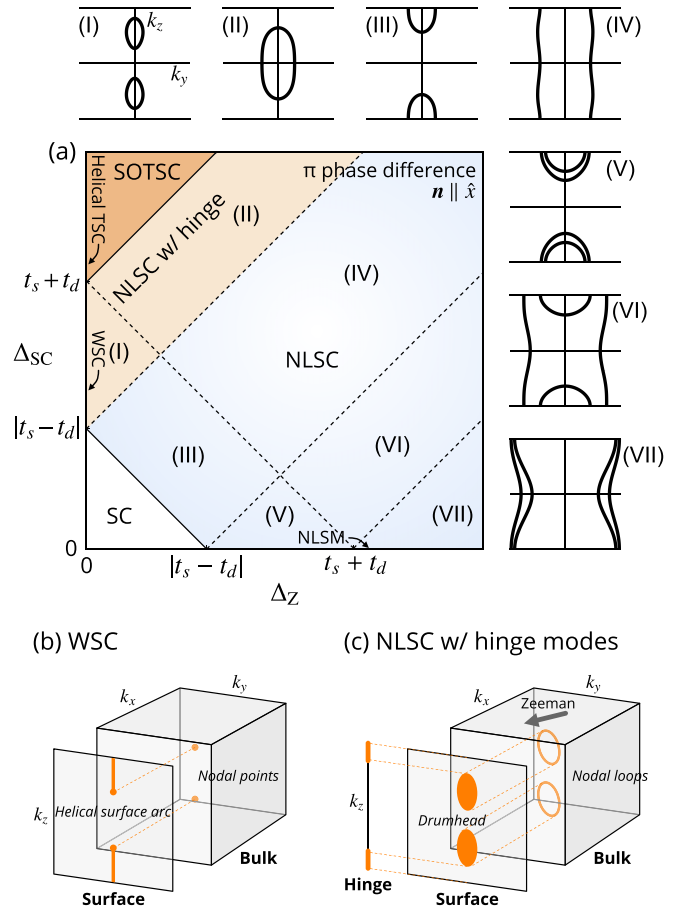


FIG. 3. (a) The phase diagram of the effective multilayer model [Fig. 1 (right)] with π phase difference in Δ_Z - Δ_{SC} space, and the shape of the line nodes in the bulk in the k_y - k_z plane. Large pair potential favors a three-dimensional second-order topological superconductor (SOTSC, the orange area) phase, while large Zeeman coupling favors nodal-line superconductor (NLSC, blue areas) phases. Between them, NLSC phases with drumhead surface modes and hinge modes (light-orange regions) appear. The position of the zero modes in the bulk, surface, and hinge in the momentum space is shown, (b) without and (c) with in-plane Zeeman coupling, which correspond to Weyl superconductor (WSC) and NLSC phases in phase (I), respectively.

at $k_z = 0$ and π in the same manner as the single-layer case. A similar situation also happens in the (II) phase in Fig. 3(a). The number of Majorana hinge modes in (I) and (II) changes continuously between the SOTSC phase and the NLSC phases (III) and (IV) without Majorana hinge modes. The (I) and (II) phases are unique to a 3D multilayer system in the sense that these phases shrink in the limit of vanishing interlayer coupling $t_d \rightarrow 0$, and the phase at each k_z section is not uniform. The origin of the Majorana hinge zero modes is the same as in the single-unit model as this multilayer model respects the same symmetries.

III. LATTICE MODEL

In this section, we consider a lattice model to observe the corner Majorana modes. In this model, the proximity effect

is incorporated as an induced pair potential on the top and bottom layers of the TI lattice.

A. Single unit

First, we consider a single unit of an SC/TI/SC layer. Consider the lattice model of the Bi₂Se₃-type TI given by [81,82]

$$\mathcal{H}_{\text{TI}}(\mathbf{k}) = \alpha(\sin k_x \sigma^x \lambda^x + \sin k_y \sigma^y \lambda^x + \sin k_z \lambda^y) + [m + t(3 - \cos k_x - \cos k_y - \cos k_z)]\lambda^z, \quad (10)$$

where σ and λ are Pauli matrices for the spin and orbital degrees of freedom, and α is the amplitude of spin-orbit coupling. By inverse Fourier transform with respect to k_z , we obtain the Hamiltonian in a slab geometry, $\mathcal{H}_{\text{TI}}(\mathbf{k}_{\perp}, z, z')$. This model shows strong TI phases when $m/t \in (-6, -4)$ and $(-2, 0)$, a weak TI phase when $m/t \in (-4, -2)$, and a trivial insulator phase otherwise. For a thin film, the 2D bulk states show a QSH phase when $m/t \in (-5, -1)$ and a trivial insulator phase otherwise. Within the QSH phase, there is a phase transition point at $m/t = -3$, where the position of the helical edge modes changes from $k = 0$ to π . We also consider Zeeman coupling and the proximity effect,

$$\mathcal{H}_Z(\mathbf{k}_{\perp}, z, z) = \Delta_Z(\mathbf{n} \cdot \boldsymbol{\sigma}), \quad (11)$$

$$\mathcal{H}_{\Delta}(\mathbf{k}_{\perp}, z, z) = \delta_{z, z_{\text{top}}} \Delta_{\text{SC}}(-\cos \varphi / 2 \sigma^y \tau^y - \sin \varphi / 2 \sigma^y \tau^x) + \delta_{z, z_{\text{bottom}}} \Delta_{\text{SC}}(-\cos \varphi / 2 \sigma^y \tau^y + \sin \varphi / 2 \sigma^y \tau^x), \quad (12)$$

where z_{top} and z_{bottom} are the position of the top and bottom surfaces of the TI lattice and τ is the Pauli matrix on the Nambu space. Here, we consider only a π junction ($\varphi = \pi$). This model has the same symmetry as the effective model in the previous section.

Without Zeeman coupling, helical TSC phases appear near the phase transition point at $m/t = -5$ and -1 [Fig. 4(a)]. The phase diagram is determined for a lattice model with three layers. The helical TSC phases near $m/t = -1$ and -5 have helical Majorana edge modes at $k = 0$ or π , respectively. Between two helical TSC phases, there are three different SC phases, each has two sets of helical Majorana modes. The momenta at which the helical Majorana modes appear are shown in Fig. 4(a).

Zeeman coupling induces a 2D SOTSC phase close to the helical TSC phases, where two or four corner Majorana zero modes appear. The number of the Majorana corner modes is equal to that of the helical Majorana edge modes without Zeeman coupling. The energy spectrum of 20×20 sites with thickness of 3 sites is shown in Fig. 4(e), where we used parameters $\alpha/t = 1$, $m/t = -5$, $\Delta_{\text{SC}}/t = 1$, $\Delta_Z/t = 0.4$, and $\mathbf{n} = (1/\sqrt{2}, 1/\sqrt{2}, 0)$. With these parameters, the bulk energy gap is $\sim 0.5t$ and Zeeman coupling opens a gap in the edge modes, leaving zero-energy Majorana corner modes. In this system, the edge gap is opened by Zeeman coupling perpendicular to the edge (e.g., the y component on the edge along x). As a result, Majorana zero modes appear at corners where the sign of the z component of $\mathbf{n} \times \mathbf{e}$ (\mathbf{e} is the unit vector parallel to the edge) changes. The position of the Majorana corner modes depends on the details of the model and is

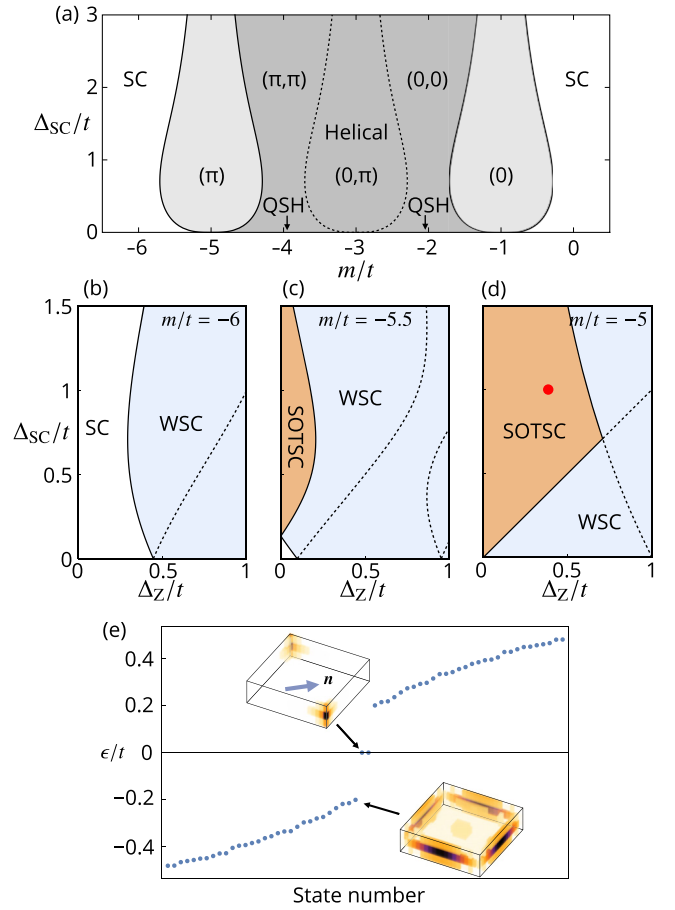


FIG. 4. (a) The phase diagram of a π junction through a three-layer TI on m - Δ_{SC} space without Zeeman coupling. Shaded regions are helical topological superconductor (TSC) phases, and the number and the position of helical edge Majorana modes are indicated. The phase diagrams with Zeeman coupling are shown on Δ_Z - Δ_{SC} space at (b) $m/t = -6$, (c) $m/t = -5.5$, and (d) $m/t = -5$. Zeeman coupling turns helical TSC phases into second-order topological superconductor (SOTSC) phases. Even larger Zeeman coupling turns them into Weyl superconductor (WSC) phases. (e) The energy spectrum at $m/t = -5$, $\Delta_{\text{SC}}/t = 1$, $\Delta_Z/t = 0.4$ [red point in (d)] and the wave function of the corner Majorana modes (inset).

different from the effective low-energy theory in the previous section and Ref. [75]. Notice that if we use another model of TI with $\cos k_z \sigma^z \lambda^x$ in place of $\cos k_z \tau^y$ in Eq. (10) (e.g., see [81]), an energy gap of the helical Majorana edge mode is opened by the orbital-dependent Zeeman coupling and the gap size is proportional to its edge-parallel component (e.g., for an edge along x , $\sigma^x \lambda^z \tau^z$). In this case, the position of the corner Majorana modes is consistent with the effective model.

The phase diagram on Δ_Z - Δ_{SC} space is shown for $m/t = -6$, -5.5 , and -5 [Figs. 4(b), 4(c), and 4(d), respectively]. Within WSC phases, dashed lines indicate phase-transition lines where the number and/or the position of the bulk Weyl nodes changes. When the phase without Zeeman coupling is a helical TSC (SC) phase, the gapped phase induced by Zeeman coupling is the SOTSC (SC) phase. The phase diagram is symmetric with respect to $m/t = -3$.

B. Multilayer

Next we consider a multilayer model of the lattice TI and SC with alternating phases on the top and bottom surfaces,

$$H = \sum_{i,j,k_{\perp},z,z'} \Psi_{ik_{\perp}z}^{\dagger} \mathcal{H}_{ij}(\mathbf{k}_{\perp}, z, z') \Psi_{jk_{\perp}z'}. \quad (13)$$

Here,

$$\begin{aligned} \mathcal{H}_{ij}(\mathbf{k}_{\perp}, z, z') &= [\mathcal{H}_{\text{TI}}(\mathbf{k}_{\perp}, z, z') + \mathcal{H}_Z(\mathbf{k}_{\perp}, z, z') + \mathcal{H}_{\Delta}(\mathbf{k}_{\perp}, z, z')] \delta_{ij} \\ &+ \frac{t_d}{2} (\delta_{i,j+1} \delta_{z,z_{\text{bottom}}} \delta_{z',z_{\text{top}}} + \delta_{i,j-1} \delta_{z,z_{\text{top}}} \delta_{z',z_{\text{bottom}}}) \lambda^z \tau^z, \end{aligned} \quad (14)$$

where i, j are the TI layer index and z is the coordinate of each layer along the stacking direction. We assume that the interlayer coupling depends on the orbital ($\propto \lambda^z$). If we employ an orbital-independent interlayer coupling ($\propto \lambda^0$), the phase diagram of the multilayer model is the same as that of the single-layer model, that is, the interlayer coupling does not work at all and each layer is independent. Notice that t in Eq. (10) is a parameter of the Hamiltonian and is independent of the thickness of the TI layer, while t_s in the effective model is the tunneling amplitude of the top and bottom surfaces and thus is dependent on the thickness.

Figure 5(a) is the phase diagram without Zeeman coupling. Here we use $t_d/t = 0.5$. The bulk phase without the proximity effect ($\Delta_{\text{SC}} = \Delta_Z = 0$) is a strong TI phase near $m/t = -5$ and -1 and a weak TI phase near $m/t = -3$. WSC phases appear between helical TSC and trivial SC phases or between helical TSC phases [Fig. 5(a)]. The Weyl nodes projected onto a surface are endpoints of a Fermi arc of helical surface Majorana modes [Fig. 3(b)]. Any two helical TSC phases separated by a WSC phase have a different number or position of the helical Majorana modes.

By including in-plane Zeeman coupling, the helical TSC phase turns to a 3D SOTSC phase and WSC phases turn to NLSC phases [Figs. 5(b)–5(d)]. The Majorana hinge modes appear in the whole k_z Brillouin zone in the SOTSC phase and within a part of the Brillouin zone in some NLSC phases. Phases with strong Zeeman coupling are mostly NLSC phases without hinge modes, which is consistent with the effective model. Dashed lines in NLSC phases represent phase transitions where the number or the shape of the nodal line changes. In an NLSC phase [the red point in Fig. 5(c)], the energy spectrum is shown for two geometries: a slab geometry with the open boundary condition (OBC) in the y direction and the periodic boundary condition (PBC) in the other directions [Fig. 5(e)], and in a geometry in Fig. 1 (right) under the OBC in both x and y directions, while the PBC in the z direction [Fig. 5(f)]. The drumhead states can be observed in the slab geometry, while the Majorana hinge modes forming a $\epsilon = 0$ flat band can be seen in the geometry in Fig. 1 (right). The hinge modes are terminated at the edge of the drumhead states as schematically shown in Fig. 3(c).

The strong and weak TI phases around $m/t = -5, -3$, and -1 retain surface Dirac cone(s) even in the presence of the weak proximity effect [green regions in Fig. 5(a)]. Small Zeeman coupling splits the surface Dirac cone(s) into two

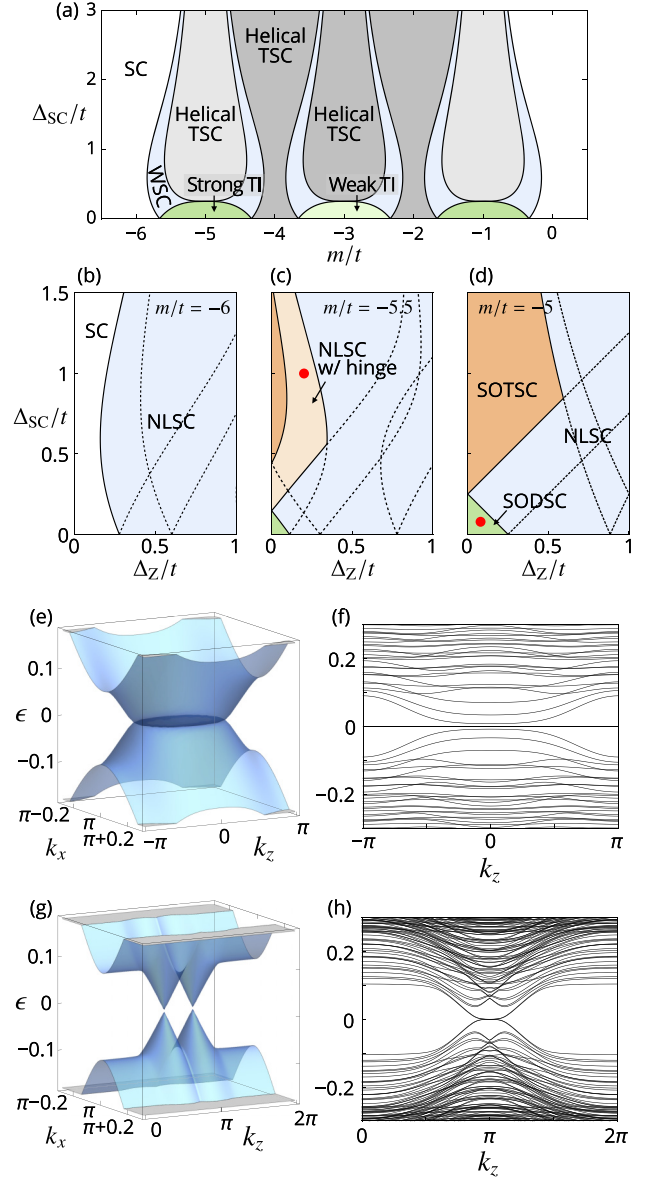


FIG. 5. (a) The phase diagram of a multilayer lattice model on m - Δ_{SC} space without Zeeman coupling. Weyl superconductor (WSC) phases intervene between SC and helical topological superconductor (TSC) phases or between helical TSC phases with different number/position of helical surface Majorana modes. Strong and weak topological insulator (TI) phases survive in the presence of a weak proximity effect. The phase diagrams with Zeeman coupling on Δ_Z - Δ_{SC} space are shown at (b) $m/t = -6$, (c) $m/t = -5.5$, and (d) $m/t = -5$. Zeeman coupling turns helical TSC phases into second-order topological superconductor (SOTSC) phases, WSC phases into nodal-line superconductor (NLSC) phases with drumhead surface modes and hinge modes, and strong TI phases into second-order Dirac superconductor (SODSC) phases. The energy spectra of a NLSC with drumhead and hinge modes [$m/t = -5.5$, $\Delta_Z/t = 0.2$, $\Delta_{\text{SC}}/t = 1$ and $\mathbf{n} = (1/\sqrt{2}, 1/\sqrt{2}, 0)$ indicated by the red point in (c)] on a slab geometry with (e) the thickness $L_y = 200$ and on geometry in Fig. 1 (right) with (f) the size $(L_x, L_y) = (40, 40)$. (g), (h) The energy spectra of an SODSC [$m/t = -5$, $\Delta_Z/t = 0.08$, and $\Delta_{\text{SC}}/t = 0.08$ indicated by the red point in (d)] on the same geometry as (e) and (f), but the size of (h) is $(L_x, L_y) = (60, 60)$.

(four) surface Majorana cones [Fig. 5(g)]. This phase is the SODSC phase [45], where two or four Majorana cones are on the surface in addition to a Majorana-zero-mode arc on the hinge connecting the surface nodes. The split of surface Majorana nodes is approximately proportional to the Zeeman field normal to the surface (e.g., on a surface normal to the y axis, the Majorana surface nodes split along the k_z direction by $\propto \Delta_Z n_y$). This phase is unique to 3D systems in the sense that there is no correspondence in 2D systems. In the geometry in Fig. 1 (right), the Majorana hinge zero modes can be seen and they connect the surface Majorana nodes [Fig. 5(h)]. From this result, the SC phase in the effective model [the SC phase around the origin in Fig. 3(a)] can be a SODSC phase. However, we could not identify this phase with our technique and we leave this problem for future work.

IV. CONCLUSION

In this paper, we studied a multilayer model of TI and SC layers where the proximity-induced pair potential has alternating signs at the top and bottom surfaces of each TI and under in-plane Zeeman coupling. In this model, we found three types of 3D HOTSC phases: (i) a SOTSC phase, each k_z section of which is a 2D SOTSC and that has Majorana hinge zero modes forming flat bands in the whole k_z space, (ii) a SODSC phase, which has surface Majorana cones and a Majorana hinge arc connecting them, and (iii) NLSC phases that have drumhead states on the surface and Majorana hinge zero modes forming arcs connecting edges of the drumhead states. The SOTSC phase appears by applying in-plane Zeeman coupling in a 3D helical TSC phase, while NLSC phases with drumhead and hinge modes emerge from WSC phases and intervene between the SOTSC phase and NLSC phases without hinge states. On the other hand, the SODSC phase appears around the strong and weak TI phases when both Zeeman coupling and the proximity effect are small. The SODSC phase and the NLSC phase with drumhead and hinge modes are unique to 3D systems.

As a lattice model, we employed Bi_2Se_3 -type TI for numerical study, but the theory could be applied to multilayers with

other TIs. In that case, the relative position of the Majorana hinge zero modes against the direction of the Zeeman field could be different from ours as it is dependent on the details of the electronic structure. From a practical perspective, a multilayer of Bi_2Se_3 could be constructed with superconducting NbSe_2 [83] or Pb [84]. In addition, since Zeeman coupling can be enhanced by doping magnetic impurities to the Bi_2Se_3 layers [85,86] and since the HOTSC phases appear in small Δ_Z regions [Figs. 5(b)–5(d)], it is enough to induce Zeeman coupling which is smaller than the induced pair potential. A small magnetic field would not disturb the proximity effect since the critical field is enhanced as SC layers are thinner, and since the motion of the surface Dirac electron is less affected by the magnetic field applied in parallel.

A π junction between neighboring SC layers could be realized by connecting them through an SC ring and by threading a magnetic flux (see Fig. 1 in Ref. [76]). When SC loops are placed vertically, the applied in-plane magnetic field generates π -phase difference and simultaneously works as an in-plane Zeeman field. Notice that once SC loops are fabricated, the π -junction condition restricts the magnetic field strength and hence in-plane Zeeman coupling. Fortunately, however, fine tuning the Zeeman coupling strength is not necessary since any of the HOTSC phases realized in our model persist down to the small Δ_Z limit [Figs. 5(b)–5(d)]. In addition, the presence of Majorana hinge flat modes, which is essential in higher-order topological phases, is considered to persist even if the phase difference is not exactly π as long as the bulk energy gap of the corresponding k_z sections remains open (see discussion for the 2D case in [75].) Notice, however, that the other Majorana modes such as the bulk nodal lines and the surface drumhead states can be subject to qualitative changes by the deviation from π .

ACKNOWLEDGMENTS

This work was supported by the Japan Society for the Promotion of Science KAKENHI (Grants No. JP17K17604 and No. JP20H01830) and by CREST, Japan Science and Technology Agency (Grant No. JPMJCR18T2).

-
- [1] A. P. Schnyder, S. Ryu, A. Furusaki, and A. W. W. Ludwig, Classification of topological insulators and superconductors in three spatial dimensions, *Phys. Rev. B* **78**, 195125 (2008).
 - [2] A. Kitaev, Periodic table for topological insulators and superconductors, *AIP Conf. Proc.* **1134**, 22 (2009).
 - [3] S. Murakami, Phase transition between the quantum spin Hall and insulator phases in 3D: Emergence of a topological gapless phase, *New J. Phys.* **9**, 356 (2007).
 - [4] X. Wan, A. M. Turner, A. Vishwanath, and S. Y. Savrasov, Topological semimetal and Fermi-arc surface states in the electronic structure of pyrochlore iridates, *Phys. Rev. B* **83**, 205101 (2011).
 - [5] A. A. Burkov and L. Balents, Weyl semimetal in a topological insulator multilayer, *Phys. Rev. Lett.* **107**, 127205 (2011).
 - [6] N. P. Armitage, E. J. Mele, and A. Vishwanath, Weyl and Dirac semimetals in three-dimensional solids, *Rev. Mod. Phys.* **90**, 015001 (2018).
 - [7] L. Fu, Topological crystalline insulators, *Phys. Rev. Lett.* **106**, 106802 (2011).
 - [8] Y. Ando and L. Fu, Topological crystalline insulators and topological superconductors: From concepts to materials, *Annu. Rev. Condens. Matter Phys.* **6**, 361 (2015).
 - [9] S. Murakami and N. Nagaosa, Berry phase in magnetic superconductors, *Phys. Rev. Lett.* **90**, 057002 (2003).
 - [10] T. Meng and L. Balents, Weyl superconductors, *Phys. Rev. B* **86**, 054504 (2012).
 - [11] S. A. Yang, H. Pan, and F. Zhang, Dirac and Weyl superconductors in three dimensions, *Phys. Rev. Lett.* **113**, 046401 (2014).
 - [12] A. P. Schnyder and P. M. R. Brydon, Topological surface states in nodal superconductors, *J. Phys.: Condens. Matter* **27**, 243201 (2015).
 - [13] C.-K. Chiu, H. Yao, and S. Ryu, Classification of topological insulators and superconductors in the presence of reflection symmetry, *Phys. Rev. B* **88**, 075142 (2013).

- [14] K. Shiozaki and M. Sato, Topology of crystalline insulators and superconductors, *Phys. Rev. B* **90**, 165114 (2014).
- [15] F. D. M. Haldane, Model for a quantum Hall effect without Landau levels: Condensed-matter realization of the “parity anomaly,” *Phys. Rev. Lett.* **61**, 2015 (1988).
- [16] C. L. Kane and E. J. Mele, Z_2 topological order and the quantum spin Hall effect, *Phys. Rev. Lett.* **95**, 146802 (2005).
- [17] N. Read and D. Green, Paired states of fermions in two dimensions with breaking of parity and time-reversal symmetries and the fractional quantum Hall effect, *Phys. Rev. B* **61**, 10267 (2000).
- [18] T. L. Hughes, E. Prodan, and B. A. Bernevig, Inversion-symmetric topological insulators, *Phys. Rev. B* **83**, 245132 (2011).
- [19] J. Zak, Berry’s phase for energy bands in solids, *Phys. Rev. Lett.* **62**, 2747 (1989).
- [20] R. D. King-Smith and D. Vanderbilt, Theory of polarization of crystalline solids, *Phys. Rev. B* **47**, 1651 (1993).
- [21] X.-L. Qi, T. L. Hughes, and S.-C. Zhang, Topological field theory of time-reversal invariant insulators, *Phys. Rev. B* **78**, 195424 (2008).
- [22] W. A. Benalcazar, B. A. Bernevig, and T. L. Hughes, Quantized electric multipole insulators, *Science* **357**, 61 (2017).
- [23] W. A. Benalcazar, B. A. Bernevig, and T. L. Hughes, Electric multipole moments, topological multipole moment pumping, and chiral hinge states in crystalline insulators, *Phys. Rev. B* **96**, 245115 (2017).
- [24] F. Schindler, A. M. Cook, M. G. Vergniory, Z. Wang, S. S. P. Parkin, B. A. Bernevig, and T. Neupert, Higher-order topological insulators, *Sci. Adv.* **4**, eaat0346 (2018).
- [25] W. A. Benalcazar, T. Li, and T. L. Hughes, Quantization of fractional corner charge in C_n -symmetric higher-order topological crystalline insulators, *Phys. Rev. B* **99**, 245151 (2019).
- [26] B. Xie, H.-X. Wang, X. Zhang, P. Zhan, J.-H. Jiang, M. Lu, and Y. Chen, Higher-order band topology, *Nat. Rev. Phys.* **3**, 520 (2021).
- [27] E. Khalaf, Higher-order topological insulators and superconductors protected by inversion symmetry, *Phys. Rev. B* **97**, 205136 (2018).
- [28] M. Serra-Garcia, V. Peri, R. Stüsstrunk, O. R. Bilal, T. Larsen, L. G. Villanueva, and S. D. Huber, Observation of a phononic quadrupole topological insulator, *Nature (London)* **555**, 342 (2018).
- [29] C. W. Peterson, W. A. Benalcazar, T. L. Hughes, and G. Bahl, A quantized microwave quadrupole insulator with topologically protected corner states, *Nature (London)* **555**, 346 (2018).
- [30] S. Imhof, C. Berger, F. Bayer, J. Brehm, L. W. Molenkamp, T. Kiessling, F. Schindler, C. H. Lee, M. Greiter, T. Neupert, and R. Thomale, Topoelectrical-circuit realization of topological corner modes, *Nat. Phys.* **14**, 925 (2018).
- [31] Z. Song, Z. Fang, and C. Fang, $(d - 2)$ -dimensional edge states of rotation symmetry protected topological states, *Phys. Rev. Lett.* **119**, 246402 (2017).
- [32] J. Langbehn, Y. Peng, L. Trifunovic, F. von Oppen, and P. W. Brouwer, Reflection-symmetric second-order topological insulators and superconductors, *Phys. Rev. Lett.* **119**, 246401 (2017).
- [33] H. Shapourian, Y. Wang, and S. Ryu, Topological crystalline superconductivity and second-order topological superconductivity in nodal-loop materials, *Phys. Rev. B* **97**, 094508 (2018).
- [34] X. Zhu, Tunable majorana corner states in a two-dimensional second-order topological superconductor induced by magnetic fields, *Phys. Rev. B* **97**, 205134 (2018).
- [35] Y. Wang, M. Lin, and T. L. Hughes, Weak-pairing higher order topological superconductors, *Phys. Rev. B* **98**, 165144 (2018).
- [36] L. Trifunovic and P. Brouwer, Bott periodicity for the topological classification of gapped states of matter with reflection symmetry, *Phys. Rev. B* **96**, 195109 (2017).
- [37] Q. Wang, C.-C. Liu, Y.-M. Lu, and F. Zhang, High-temperature Majorana corner states, *Phys. Rev. Lett.* **121**, 186801 (2018).
- [38] Y. Peng and Y. Xu, Proximity-induced Majorana hinge modes in antiferromagnetic topological insulators, *Phys. Rev. B* **99**, 195431 (2019).
- [39] M. Geier, L. Trifunovic, M. Hoskam, and P. W. Brouwer, Second-order topological insulators and superconductors with an order-two crystalline symmetry, *Phys. Rev. B* **97**, 205135 (2018).
- [40] Z. Yan, Majorana corner and hinge modes in second-order topological insulator/superconductor heterostructures, *Phys. Rev. B* **100**, 205406 (2019).
- [41] N. Bultinck, B. A. Bernevig, and M. P. Zaletel, Three-dimensional superconductors with hybrid higher-order topology, *Phys. Rev. B* **99**, 125149 (2019).
- [42] Z. Wu, Z. Yan, and W. Huang, Higher-order topological superconductivity: Possible realization in Fermi gases and Sr_2RuO_4 , *Phys. Rev. B* **99**, 020508(R) (2019).
- [43] B. Roy, Anticommuting symmetry protected higher-order topological phases, *Phys. Rev. Res.* **1**, 032048(R) (2019).
- [44] R. Okugawa, S. Hayashi, and T. Nakanishi, Second-order topological phases protected by chiral symmetry, *Phys. Rev. B* **100**, 235302 (2019).
- [45] S. A. A. Ghorashi, X. Hu, T. L. Hughes, and E. Rossi, Second-order Dirac superconductors and magnetic field induced Majorana hinge modes, *Phys. Rev. B* **100**, 020509(R), (2019).
- [46] R.-X. Zhang, W. S. Cole, and S. Das Sarma, Helical hinge Majorana modes in iron-based superconductors, *Phys. Rev. Lett.* **122**, 187001 (2019).
- [47] R.-X. Zhang, W. S. Cole, X. Wu, and S. Das Sarma, Higher-order topology and nodal topological superconductivity in $\text{Fe}(\text{Se}, \text{Te})$ heterostructures, *Phys. Rev. Lett.* **123**, 167001 (2019).
- [48] R. Queiroz and A. Stern, Splitting the hinge mode of higher-order topological insulators, *Phys. Rev. Lett.* **123**, 036802 (2019).
- [49] B. Roy, Higher-order topological superconductors in \mathcal{P} -, \mathcal{T} -odd quadrupolar Dirac materials, *Phys. Rev. B* **101**, 220506(R) (2020).
- [50] R. W. Bomantara, Time-induced second-order topological superconductors, *Phys. Rev. Res.* **2**, 033495 (2020).
- [51] A. K. Ghosh, T. Nag, and A. Saha, Floquet generation of a second-order topological superconductor, *Phys. Rev. B* **103**, 045424 (2021).
- [52] A. K. Ghosh, T. Nag, and A. Saha, Hierarchy of higher-order topological superconductors in three dimensions, *Phys. Rev. B* **104**, 134508 (2021).
- [53] B. Roy and V. Juričić, Mixed-parity octupolar pairing and corner Majorana modes in three dimensions, *Phys. Rev. B* **104**, L180503 (2021).

- [54] M. Kheirkhah, Z.-Y. Zhuang, J. Maciejko, and Z. Yan, Surface Bogoliubov-Dirac cones and helical Majorana hinge modes in superconducting Dirac semimetals, *Phys. Rev. B* **105**, 014509 (2022).
- [55] A. D. Fedoseev, Higher-order topological superconductor on the bipartite triangular lattice, *Phys. Rev. B* **105**, 155423 (2022).
- [56] S. A. A. Ghorashi, J. Cano, E. Rossi, and T. L. Hughes, Higher-order nodal hinge states in doped superconducting topological insulator, *Phys. Rev. B* **108**, 094504 (2023).
- [57] A. Chew, Y. Wang, B. A. Bernevig, and Z.-D. Song, Higher-order topological superconductivity in twisted bilayer graphene, *Phys. Rev. B* **107**, 094512 (2023).
- [58] R.-X. Zhang, Bulk-vortex correspondence of higher-order topological superconductors (unpublished).
- [59] M. Kheirkhah, Z. Yan, and F. Marsiglio, Vortex-line topology in iron-based superconductors with and without second-order topology, *Phys. Rev. B* **103**, L140502 (2021).
- [60] Z. Wu and Y. Wang, Nodal higher-order topological superconductivity from a \mathcal{C}_4 -symmetric Dirac semimetal, *Phys. Rev. B* **106**, 214510 (2022).
- [61] C. Nayak, S. H. Simon, A. Stern, M. Freedman, and S. Das Sarma, Non-Abelian anyons and topological quantum computation, *Rev. Mod. Phys.* **80**, 1083 (2008).
- [62] Z. Yan, F. Song, and Z. Wang, Majorana corner modes in a high-temperature platform, *Phys. Rev. Lett.* **121**, 096803 (2018).
- [63] T. Liu, J. J. He, and F. Nori, Majorana corner states in a two-dimensional magnetic topological insulator on a high-temperature superconductor, *Phys. Rev. B* **98**, 245413 (2018).
- [64] C.-H. Hsu, P. Stano, J. Klinovaja, and D. Loss, Majorana Kramers pairs in higher-order topological insulators, *Phys. Rev. Lett.* **121**, 196801 (2018).
- [65] X.-H. Pan, K.-J. Yang, L. Chen, G. Xu, C.-X. Liu, and X. Liu, Lattice-symmetry-assisted second-order topological superconductors and Majorana patterns, *Phys. Rev. Lett.* **123**, 156801 (2019).
- [66] Y.-J. Wu, J. Hou, Y.-M. Li, X.-W. Luo, X. Shi, and C. Zhang, In-plane Zeeman-field-induced Majorana corner and hinge modes in an *s*-wave superconductor heterostructure, *Phys. Rev. Lett.* **124**, 227001 (2020).
- [67] Y.-J. Wu, W. Tu, and N. Li, Majorana corner states in an attractive quantum spin Hall insulator with opposite in-plane Zeeman energy at two sublattice sites, *J. Phys.: Condens. Matter* **34**, 375601 (2022).
- [68] B. Lu and Y. Zhang, Tunable Majorana corner modes by orbital-dependent exchange interaction in a two-dimensional topological superconductor, *J. Phys.: Condens. Matter* **34**, 305302 (2022).
- [69] X.-T. Chen, C.-H. Liu, D.-H. Xu, and C.-Z. Chen, Majorana corner modes and flat-band majorana edge modes in superconductor/topological-insulator/superconductor junctions, *Chinese Phys. Lett.* **40**, 097403 (2023).
- [70] X. Zhu, Second-order topological superconductors with mixed pairing, *Phys. Rev. Lett.* **122**, 236401 (2019).
- [71] M. Kheirkhah, Z. Yan, Y. Nagai, and F. Marsiglio, First- and second-order topological superconductivity and temperature-driven topological phase transitions in the extended Hubbard model with spin-orbit coupling, *Phys. Rev. Lett.* **125**, 017001 (2020).
- [72] K. Laubscher, D. Chughtai, D. Loss, and J. Klinovaja, Kramers pairs of Majorana corner states in a topological insulator bilayer, *Phys. Rev. B* **102**, 195401 (2020).
- [73] K. Yokomizo and S. Murakami, Topological phases in a Weyl semimetal multilayer, *Phys. Rev. B* **95**, 155101 (2017).
- [74] R. Nakai and K. Nomura, Weyl superconductor phases in a Weyl-semimetal/superconductor multilayer, *Phys. Rev. B* **101**, 094510 (2020).
- [75] Y. Volpez, D. Loss, and J. Klinovaja, Second-order topological superconductivity in π -junction Rashba layers, *Phys. Rev. Lett.* **122**, 126402 (2019).
- [76] T. Meng and L. Balents, Erratum: Weyl superconductors [*Phys. Rev. B* **86**, 054504 (2012)], *Phys. Rev. B* **96**, 019901(E) (2017).
- [77] C.-X. Liu and B. Trauzettel, Helical Dirac-Majorana interferometer in a superconductor/topological insulator sandwich structure, *Phys. Rev. B* **83**, 220510(R) (2011).
- [78] C.-X. Liu, H.-J. Zhang, B. Yan, X.-L. Qi, T. Frauenheim, X. Dai, Z. Fang, and S.-C. Zhang, Oscillatory crossover from two-dimensional to three-dimensional topological insulators, *Phys. Rev. B* **81**, 041307(R) (2010).
- [79] L. Fu and C. L. Kane, Josephson current and noise at a superconductor/quantum-spin-Hall-insulator/superconductor junction, *Phys. Rev. B* **79**, 161408(R) (2009).
- [80] X.-L. Qi, T. L. Hughes, and S.-C. Zhang, Chiral topological superconductor from the quantum Hall state, *Phys. Rev. B* **82**, 184516 (2010).
- [81] C.-X. Liu, X.-L. Qi, H.-J. Zhang, X. Dai, Z. Fang, and S.-C. Zhang, Model Hamiltonian for topological insulators, *Phys. Rev. B* **82**, 045122 (2010).
- [82] R. Li, J. Wang, X.-L. Qi, and S.-C. Zhang, Dynamical axion field in topological magnetic insulators, *Nat. Phys.* **6**, 284 (2010).
- [83] J.-P. Xu, M.-X. Wang, Z. L. Liu, J.-F. Ge, X. Yang, C. Liu, Z. A. Xu, D. Guan, C. L. Gao, D. Qian, Y. Liu, Q.-H. Wang, F.-C. Zhang, Q.-K. Xue, and J.-F. Jia, Experimental detection of a Majorana mode in the core of a magnetic vortex inside a topological insulator-superconductor $\text{Bi}_2\text{Te}_3/\text{NbSe}_2$ heterostructure, *Phys. Rev. Lett.* **114**, 017001 (2015).
- [84] C. X. Trang, N. Shimamura, K. Nakayama, S. Souma, K. Sugawara, I. Watanabe, K. Yamauchi, T. Oguchi, K. Segawa, T. Takahashi, Y. Ando, and T. Sato, Conversion of a conventional superconductor into a topological superconductor by topological proximity effect, *Nat. Commun.* **11**, 159 (2020).
- [85] R. Yu, W. Zhang, H.-J. Zhang, S.-C. Zhang, X. Dai, and Z. Fang, Quantized anomalous Hall effect in magnetic topological insulators, *Science* **329**, 61 (2010).
- [86] Y. L. Chen, J.-H. Chu, J. G. Analytis, Z. K. Liu, K. Igarashi, H.-H. Kuo, X. L. Qi, S. K. Mo, R. G. Moore, D. H. Lu, M. Hashimoto, T. Sasagawa, S. C. Zhang, I. R. Fisher, Z. Hussain, and Z. X. Shen, Massive Dirac fermion on the surface of a magnetically doped topological insulator, *Science* **329**, 659 (2010).